(Received 16 March 2026, Accepted 12 May 2026, Scheduled 22 May 2026)

Design and Isolation Enhancement of a Compact Reconfigurable Dual-Band MIMO Antenna

Jie Sun[1,2], Hucheng Sun[1,2], and Yan Li[1,2,*]

[1]*Jiangsu Collaborative Innovation Center of Atmospheric Environment and Equipment Technology Nanjing University of Information Science and Technology, Nanjing 210044, China*
[2]*Research Center of Applied Electromagnetics, Nanjing University of Information Science and Technology, Nanjing 210044, China*

ABSTRACT: This paper presents a compact dual-band reconfigurable MIMO antenna array that simultaneously addresses the challenges of frequency agility and strong inter-element coupling in densely integrated antennas. The proposed antenna element employs a slit-loaded microstrip patch combined with a varactor diode to achieve continuous tuning of the high-frequency band while maintaining a stable low-frequency resonance. To suppress the severe mutual coupling typically induced by reconfigurable structures, an optimized etched ground-plane topology featuring branched Π-shaped slots is introduced. This isolation structure effectively alters surface-wave propagation paths and attenuates coupling fields, resulting in a significant improvement in port-to-port isolation across both operating bands. Comprehensive parametric studies validate the effectiveness of the slot configuration in enhancing decoupling performance under various tuning states. A 1×4 MIMO array prototype was fabricated and experimentally evaluated, showing good agreement with simulations. Measurements demonstrate wide-range high-band tuning from 3.6 to 4.2 GHz, stable low-band operation near 2.3 GHz, improved radiation efficiency, and low envelope correlation coefficients, confirming strong diversity performance. Owing to its compact structure, stable dual-band characteristics, and robust reconfigurability, the proposed design offers a promising solution for adaptive and space-constrained modern wireless communication systems.

1. INTRODUCTION

The rapid evolution of modern wireless communication systems has created an urgent demand for antenna technologies capable of providing dynamic spectrum access, multi-band operability, and high data throughput within compact device structures [1–4]. As wireless standards continue to diversify and frequency resources become increasingly fragmented, antennas must support agile frequency tuning without compromising radiation performance or system reliability. Multiple-input–multiple-output (MIMO) technology [5–7] has emerged as a key enabling technique for enhancing channel capacity and link robustness by exploiting spatial multiplexing and diversity. However, integrating multiple antenna elements into a limited device structure presents notable challenges. These include severe inter-element coupling, degraded radiation efficiency, and increased correlation between antenna ports [8–10]. All of them adversely affect the overall performance of the MIMO system.

Reconfigurable antennas have gained significant attention in recent years due to their ability to adapt operational frequencies or radiation patterns dynamically through electronically tunable components such as varactor diodes, PIN diodes, and RF MEMS switches [11–13]. Such capability is particularly useful for multi-standard wireless devices and spectrum-sharing networks. Despite their advantages, integrating reconfigurable structures into MIMO systems introduces additional design difficulties [14–16]. Tuning components often modify the surface current distribution, thereby aggravating electromagnetic coupling between closely spaced elements. As a result, achieving both wide-range reconfigurability and high inter-port isolation becomes a conflicting design requirement that continues to limit the practicality of compact reconfigurable MIMO antennas.

To mitigate the coupling issue, numerous decoupling and isolation-enhancement methods have been explored. Conventional techniques include neutralization lines, parasitic elements, and orthogonal mode excitation, each offering specific benefits but also inheriting limitations in terms of bandwidth, structural complexity, or sensitivity to tuning states [17–22]. Some other solutions, such as defected ground structures (DGS) and electromagnetic bandgap (EBG) configurations [23–25], have demonstrated improved suppression of surface waves and near-field coupling. For example, etched slot patterns in the ground plane can redirect coupling currents and introduce band-stop characteristics near operational frequencies. Similarly, DGS and EBG units can create high-impedance surfaces to reduce unwanted field interactions. However, these approaches often require large areas or periodic structures, making them less suitable for compact, densely packed MIMO arrays. Moreover, reconfigurable MIMO systems impose additional constraints because tuning components shift resonance conditions, causing isolation structures to lose effectiveness unless they are specifically optimized for multiple operating states [26–31].

* Corresponding author: Yan Li (liyan11@nuist.edu.cn).

Motivated by these challenges, this work proposes a compact dual-band reconfigurable MIMO antenna array that simultaneously achieves dynamic high-frequency tuning and strong inter-element isolation. The antenna element employs a slit-loaded rectangular microstrip patch integrated with a varactor diode, enabling continuous tuning across the upper frequency band while maintaining a stable and robust lower band. To address the inherent coupling introduced by reconfigurable structures, an innovative etched ground-plane isolation mechanism is developed. The proposed branched Π-shaped slot topology is carefully optimized to reshape surface current paths, suppress mutual coupling, and maintain high isolation across both frequency bands under various biasing conditions. Unlike conventional DGS-based approaches, the introduced structure offers directional suppression of coupling fields with minimal impact on impedance matching and minimal occupation of physical space. Comprehensive electromagnetic simulations and parametric analyses reveal the interplay among slot geometry, positioning, tuning states, and isolation performance. A 1×4 MIMO prototype is fabricated to validate the proposed design experimentally. Measured results demonstrate stable low-band operation, wide-range high-band tunability, improved radiation efficiency, and significantly enhanced isolation in both bands. Additionally, low envelope correlation coefficients (ECC) confirm the design's suitability for high-capacity MIMO applications. Overall, the proposed reconfigurable dual-band MIMO antenna array presents a compact, efficient, and robust solution for next-generation adaptive wireless systems, offering a balanced combination of spectral flexibility, high isolation, and practical implementation feasibility.

2. ANTENNA ELEMENT DESIGN

The proposed antenna element is designed to achieve compact size, dual-band operation, and continuous high-frequency tuning while maintaining stable low-frequency performance. Fig. 1 illustrates the structure of the element, which is implemented on a 3-mm-thick FR4 substrate ($\varepsilon_r = 4.4$, $\tan\delta = 0.02$). A conventional rectangular microstrip patch serves as the foundation of the radiating structure. To enable dual-band characteristics and introduce reconfigurability, a narrow vertical slit is etched along the central axis of the patch, dividing it into two electrically connected regions. This slit perturbs the original current distribution, effectively generating an additional resonance mode at a lower frequency. The slit also increases the effective current path length, which contributes to stable low-band operation near 2.4 GHz. To ensure reliable RF current continuity across the divided patch, four low-loss chip capacitors (68 nF) are strategically placed along the slit. Electromagnetic simulations demonstrate that these capacitors suppress undesirable local current interruptions and prevent high-frequency gain degradation, especially when the upper resonance is tuned through varactor loading. The placement and capacitance values were determined through iterative parametric studies in Ansys High Frequency Structure Simulator (HFSS), confirming that distributed capacitive bridging offers better frequency stability than a single large capacitor.

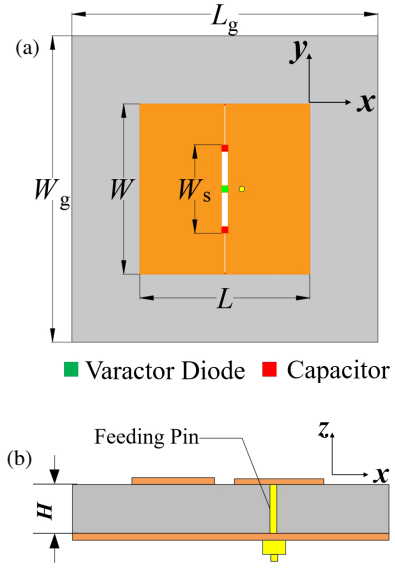

FIGURE 1. Structure of the proposed antenna element. (a) Top view. (b) Side view.

A key feature enabling frequency reconfigurability is the integration of a varactor diode (SMV1430) at the midpoint of the slit. The diode provides a tunable capacitance range of approximately 0.31–1.24 pF when the DC bias varies from 0 to 30 V. By embedding the varactor directly into the electric-field maximum region associated with the high-frequency mode, the antenna's upper resonance can be shifted continuously. The bias line is routed along the left half of the patch and isolated through a 180-nH RF choke, ensuring negligible interference with the radio frequency (RF) signal path. Meanwhile, the biasing circuit maintains high impedance at operational frequencies, minimizing unwanted radiation or pattern distortion.

Parametric optimization was conducted to determine the final geometric dimensions listed in Table 1. Parameters such as the slit width, overall patch dimension, and the location of the capacitive bridges were adjusted to guarantee strong coupling between the varactor-dominated tuning mode and the natural resonance of the patch. Under optimal configuration, the low-frequency band remains nearly insensitive to varactor tuning, with deviation less than 2% across all bias conditions. This behavior results from the fact that the low-band mode is primarily dominated by the longer current path around the outer edges of the patch rather than the slit region.

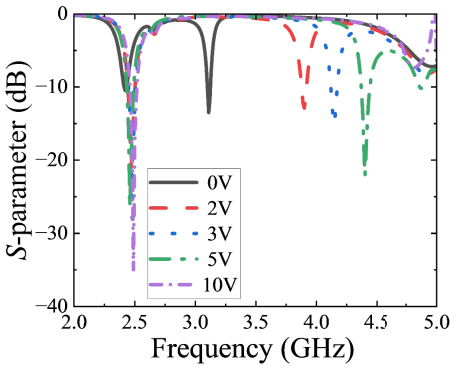

FIGURE 2. Simulated S-parameters of the antenna element.

TABLE 1. Dimensions of the antenna element.

Parameter	Value (mm)	Parameter	Value (mm)	Parameter	Value (mm)
L_g	45	W_g	45	W_s	13
L	25	W	25	H	3

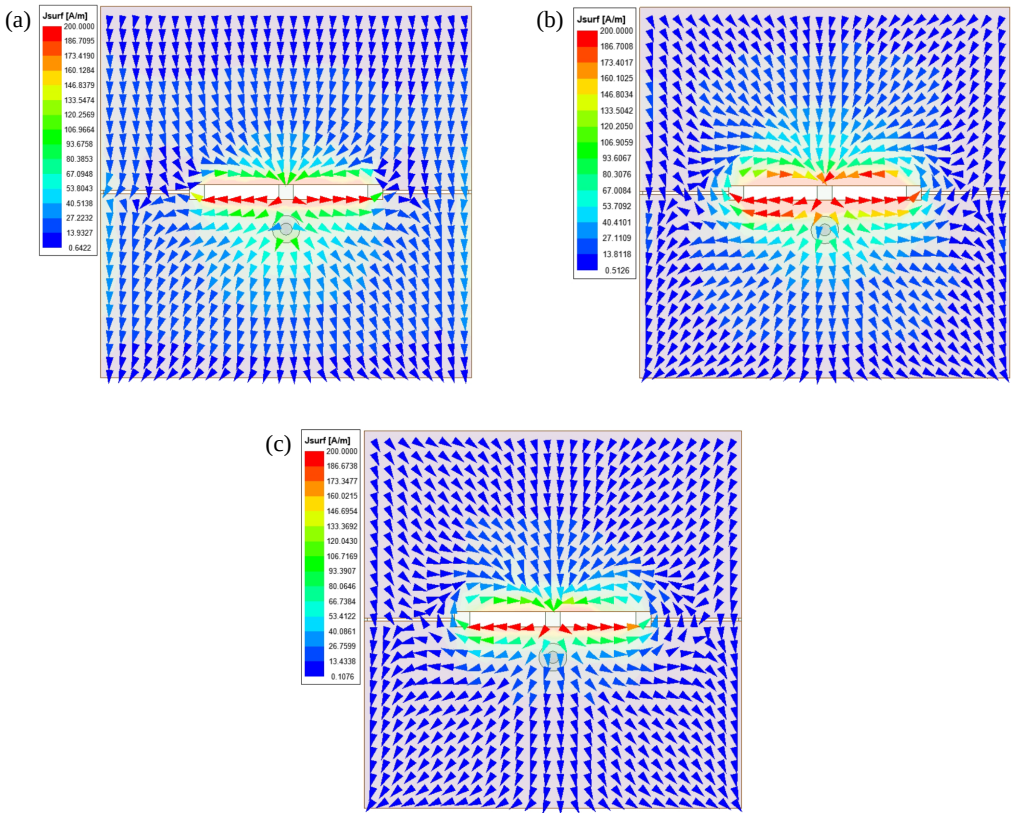

FIGURE 3. Simulated surface current distributions of the proposed antenna element under the DC bias voltages of (a) 0 V, (b) 3 V, and (c) 5 V.

Figure 2 shows the simulated S-parameters under different DC bias voltages. As the bias increases, the varactor capacitance decreases, shifting the high-frequency resonance smoothly from 3.3 to 4.6 GHz. The tuning range is sufficiently wide to accommodate multiple upper-band wireless standards, including sub-6 GHz 5G, WLAN, and emerging mid-band reconfigurable applications. Throughout the tuning range, impedance matching remains well controlled, indicating strong interaction between the slit-induced mode and the varactor-loaded resonance.

As the DC bias voltage increases, the capacitance value of the varactor diode exhibits a decreasing trend, leading to a significant increase in phase shift. However, the phase shift required for the antenna to operate in the high-frequency band needs to remain constant. To maintain a constant phase shift value, the frequency must be increased, resulting in a simultaneous increase in the antenna's resonant frequency as the DC bias voltage increases. This phenomenon is consistent with the pattern presented in Fig. 2. In the high-frequency band, as the DC bias voltage increases, the antenna's operating frequency also shifts toward higher frequency bands.

This study selected typical cases with DC bias voltages of 0 V, 3 V, and 5 V for analysis, with corresponding operating frequencies of 3.2 GHz, 4.2 GHz, and 4.4 GHz, respectively. Surface current distributions of the antenna element under different DC bias voltages are drawn, as shown in Fig. 3. Analysis shows that despite differences in DC bias voltage, the antenna's surface current distribution still exhibits similar distribution characteristics, indicating consistency in its operating mode. The differences in phase shift caused by the varactor diode at different voltages can be effectively compensated through adaptive adjustment of the resonant frequency.

Simulated normalized radiation patterns of the antenna element are evaluated in Fig. 4. At both operating frequencies, the antenna exhibits stable patterns resembling those of a traditional microstrip patch. At 2.4 GHz, the radiation pattern is broadside with low cross-polarization in both the *xoz*- and *yoz*-planes. At 4.1 GHz, although the electrical size of the patch increases, the broadside radiation remains consistent without significant beam tilting, demonstrating robust modal behavior across tuning states. The peak gain reaches 3.7 dBi and 5.2 dBi for the low and high bands, respectively, making the element

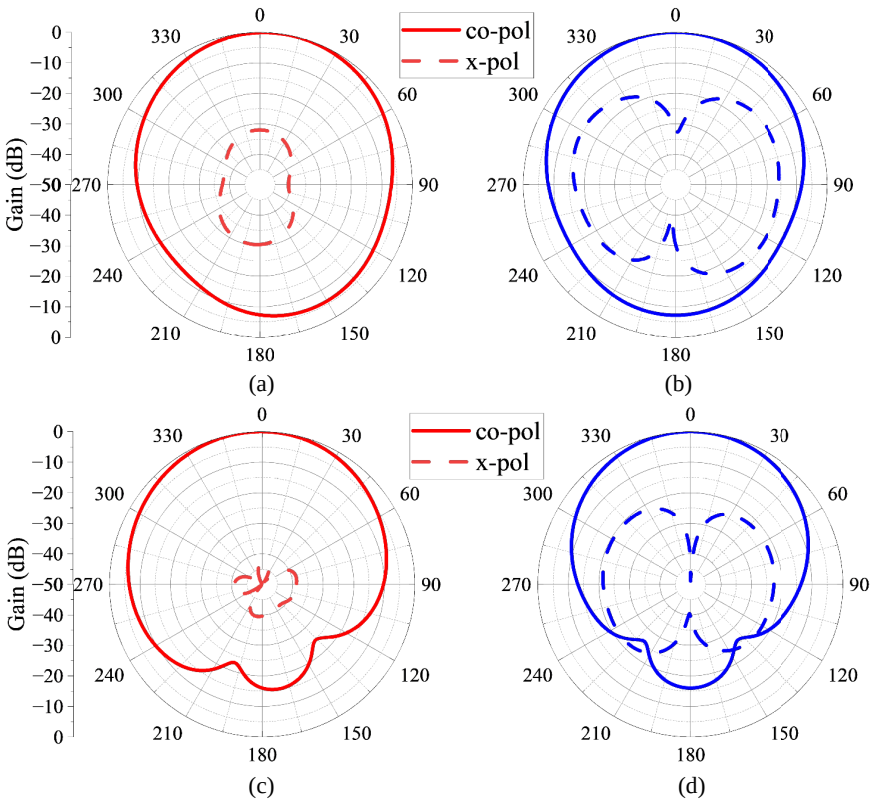

FIGURE 4. Simulated normalized radiation patterns of the antenna element. (a) At 2.4 GHz in *xoz*-plane. (b) At 2.4 GHz in *yoz*-plane. (c) At 4.1 GHz in *xoz*-plane. (d) At 4.1 GHz in *xoz*-plane.

suitable for array applications. In summary, the antenna element combines slit-loaded miniaturization, varactor-tuned reconfigurability, and capacitive stabilization to achieve compact dual-band operation with strong frequency agility. This element serves as the foundation for constructing the reconfigurable MIMO array discussed in the following sections.

3. RECONFIGURABLE DUAL-BAND MIMO ANTENNA DESIGN

To meet the requirements of compact integration and dual-band frequency agility, a 1×4 MIMO antenna array is constructed using the reconfigurable dual-band antenna elements described in the last section. The primary design objective is to preserve the tunable high-frequency resonance while ensuring robust isolation between closely spaced antenna elements. This section details the design methodology, isolation-enhancement strategy, parametric optimization, and electromagnetic behavior of the proposed MIMO configuration.

The array layout is illustrated in Fig. 5. The four antenna elements are arranged linearly along the x-axis, sharing the same FR4 substrate and ground plane. Due to the compact physical spacing, strong mutual coupling naturally arises through some primary mechanisms. The surface-wave propagation is supported by the dielectric substrate. The near-field coupling is dominated by electric fields around the slit-loaded patches, and the space-wave interaction is caused by the broadside radiating patterns of adjacent elements. In particular, the presence of

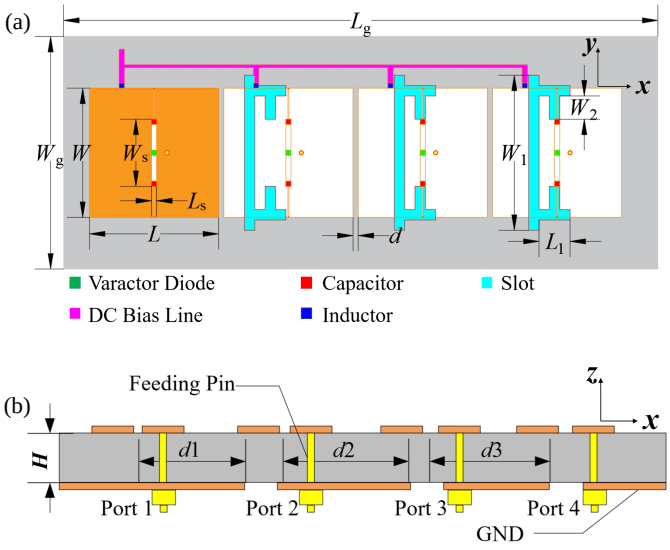

FIGURE 5. Structure of the proposed 1×4 MIMO antenna array. (a) Top view. (b) Side view.

a varactor diode and capacitive bridges redistributes the patch surface currents, increasing the sensitivity of coupling paths to frequency tuning. As a result, conventional MIMO isolation strategies become ineffective unless specifically designed to accommodate this multi-state behavior.

To address this challenge, a branched Π-shaped slot structure is etched onto the ground plane below the four elements. As shown in Fig. 5(b), three identical Π-slot units are positioned

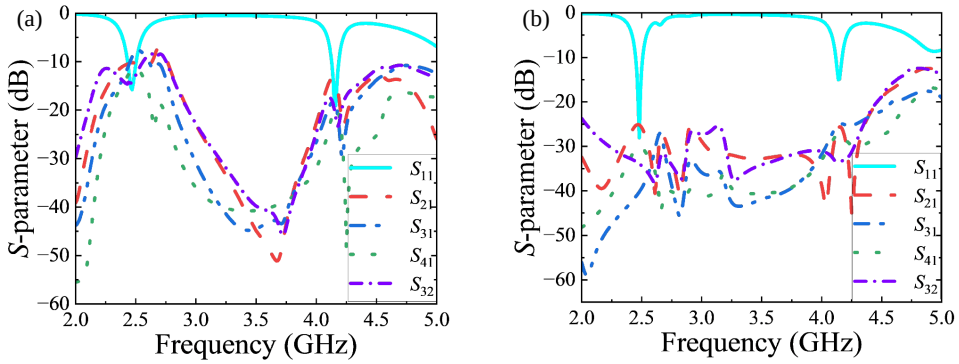

FIGURE 6. Simulated S-parameters of the MIMO antenna array under the bias DC voltage of 3 V. (a) Without an isolation slot. (b) With an isolation slot.

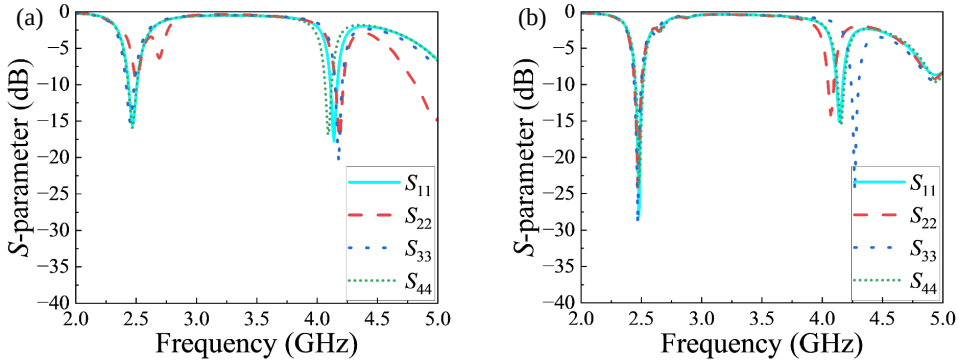

FIGURE 7. Simulated reflection coefficients of the MIMO antenna array under the bias DC voltage of 3 V. (a) Without an isolation slot. (b) With an isolation slot.

symmetrically between adjacent antenna elements. Each Π-slot consists of two vertical branches connected by a horizontal slot, forming a resonant cavity that interacts with the dominant surface currents on the ground plane. The slot topology is purposely chosen for its ability to generate directional current suppression, thereby interrupting the dominant coupling pathways without significantly modifying the reflection characteristics of individual antenna elements.

The isolation mechanism can be explained through electromagnetic field interactions. In the absence of slots, strong surface currents flow along the ground plane, particularly between the feed locations of adjacent antenna elements. These currents contribute heavily to S_{21} and S_{31} coupling. When the Π-slot is introduced, the abrupt discontinuity alters the propagation constant of surface waves. The slot acts as a band-stop resonator near both the low- and high-frequency operating bands, increasing the effective inductance and capacitance of the ground current path. This creates a high-impedance barrier that limits current transmission between elements. Additionally, the branched geometry enables multi-band suppression by supporting multiple current modes within the slot cavity, improving its suitability for reconfigurable dual-band operation.

Simulated S-parameter comparisons are shown in Fig. 6. Without isolation slots, S_{21} in the low-frequency band is worse than -10 dB, far below acceptable MIMO performance requirements. High-frequency coupling is somewhat lower due to reduced electrical size. However, isolation still fails to exceed -20 dB. After integrating the Π-slot structures, isolation improves significantly for both operating bands. In the low-frequency region, S_{21} drops from about -8 dB to below -20 dB, demonstrating a 12 dB improvement. High-frequency isolation similarly surpasses the 20 dB threshold across the tuning range. This stable improvement confirms that the proposed slot topology effectively suppresses coupling regardless of bias-induced frequency shift. Fig. 7 shows the reflection coefficients of the MIMO array. It is evident that after incorporating the isolation slot, the reflection coefficients of the MIMO array at its four ports remain satisfactory.

To further understand the influence of structural parameters, extensive optimization is conducted on key geometric variables, such as slot width W_1, slot length, and the spacings between elements d_1, d_2, and d_3. Fig. 8 highlights the sensitivity of isolation to W_1. A narrow slot $W_1 = 25$ mm provides insufficient suppression because its resonant mode fails to overlap effectively with the coupling-dominant surface-wave mode. Increasing W_1 to 30 mm enhances its interaction with ground currents, reducing S_{21} below -24 dB across both bands. When W_1 is further increased to 35 mm, isolation performance converges, indicating that overly wide slots do not significantly enhance suppression and may introduce unnecessary perturbations to radiation patterns. Thus, $W_1 = 30$ mm is selected as the optimal width.

Similarly, Fig. 9 shows the effect of adjusting d_1, the horizontal offset of the Π-slot relative to the feed point. The

TABLE 2. Dimensions of the MIMO antenna array.

Parameter	Value (mm)	Parameter	Value (mm)	Parameter	Value (mm)
W_g	45	W	25	W_s	13
L	25	L_s	1	H	3
L_g	115	W_1	30	W_2	4
d_1	17.5	d_2	20.5	d_3	20.5

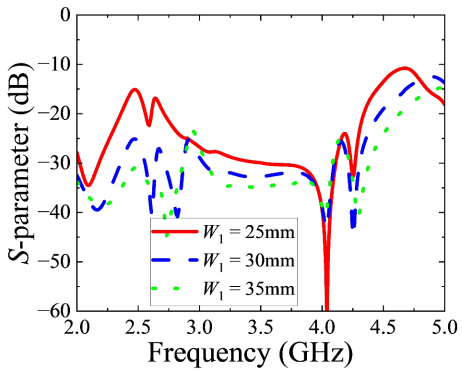

FIGURE 8. Simulated S-parameters of the MIMO antenna array with different W_1 values under the bias DC voltage of 3 V.

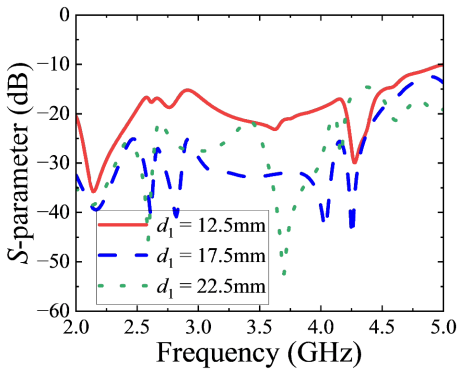

FIGURE 9. Simulated S-parameters of the MIMO antenna array with different d_1 values under the bias DC voltage of 3 V.

slot resonance must coincide with high-current-density regions on the ground plane to provide effective suppression. When $d_1 = 12.5$ mm, the slot is positioned too close to the centerline, resulting in insufficient decoupling. At $d_1 = 17.5$ mm, the slot intersects the strongest surface current path, maximizing coupling reduction. When d_1 is increased to 22.5 mm, the slot shifts away from the dominant field region, causing isolation performance to plateau. Based on multi-state performance evaluation, $d_1 = 17.5$ mm is chosen. Following this optimization methodology, all dimensional parameters are finalized and listed in Table 2.

The value of W_1 is critical in determining the resonant frequency of the Π-shaped slot structure. The selection of $W_1 = 30$ mm is attributed to its ability to tune the LC resonance of the slot to match the operating bands (2.4 GHz and 3.6–4.2 GHz). At this dimension, the slot acts as a high-impedance surface or a band-stop filter, effectively suppressing the propagation of surface waves that cause mutual coupling. A narrower width results in a resonant frequency that is too high, whereas a wider width shifts the resonance too low; neither scenario optimally covers the target bands.

The optimization of parameter d_1 is based on the spatial distribution of surface currents on the ground plane. The choice of $d_1 = 17.5$ mm corresponds to the location of maximum surface current density between adjacent elements. Positioning the slot at this specific offset maximizes the disruption of the dominant coupling path. This stands in contrast to positioning it at current nulls, which results in negligible interaction.

The surface current distributions of the antenna array with and without slots are provided in Fig. 10. The comparison clearly demonstrates that the proposed isolation scheme effectively suppresses the surface current flow between antenna elements. The E-field distributions of the array antenna with and without slots are drawn in Fig. 11. A visual comparison clearly reveals that the proposed isolation scheme effectively mitigates the E-field interference between elements, thereby achieving a significant improvement in isolation.

The correlation level between MIMO antenna elements can be characterized by the envelope correlation coefficient (ECC), where lower ECC values indicate reduced inter-element correlation and enhanced MIMO system performance. The ECC value is calculated using

$$\mathrm{ECC} = \frac{\iint_{4\pi} \left|\overline{F_i}(\theta,\phi) \times \overline{F_j}(\theta,\phi) d\Omega\right|^2}{\iint_{4\pi} \left|\overline{F_i}(\theta,\phi)\right|^2 d\Omega \iint_{4\pi} \left|\overline{F_j}(\theta,\phi)\right|^2 d\Omega} \quad (1)$$

The ECC, shown in Fig. 12(a), further verifies the effectiveness of the MIMO design. ECC values below 0.15 in the low-frequency band and below 0.02 in the high-frequency band indicate low spatial correlation and high diversity gain. Notably, ECC remains stable across different bias voltages (3–5 V), confirming that the isolation mechanism is robust against tuning-induced changes in current distribution. Fig. 12(b) illustrates the Diversity Gain (DG) of the MIMO antenna. It can be observed that the DG significantly exceeds 9.9 dB across different bias voltages (3–5 V), indicating that the antenna achieves good diversity performance. Fig. 12(c) presents the Total Active Reflection Coefficient (TARC). As shown, the TARC remains below -10 dB within the operating frequency band, demonstrating the favorable overall performance of the antenna.

It is important to note that the proposed design achieves high isolation without sacrificing tuning performance. Because the Π-shaped slots are located on the ground plane rather than the patch surface, they do not interfere with the varactor-dominated

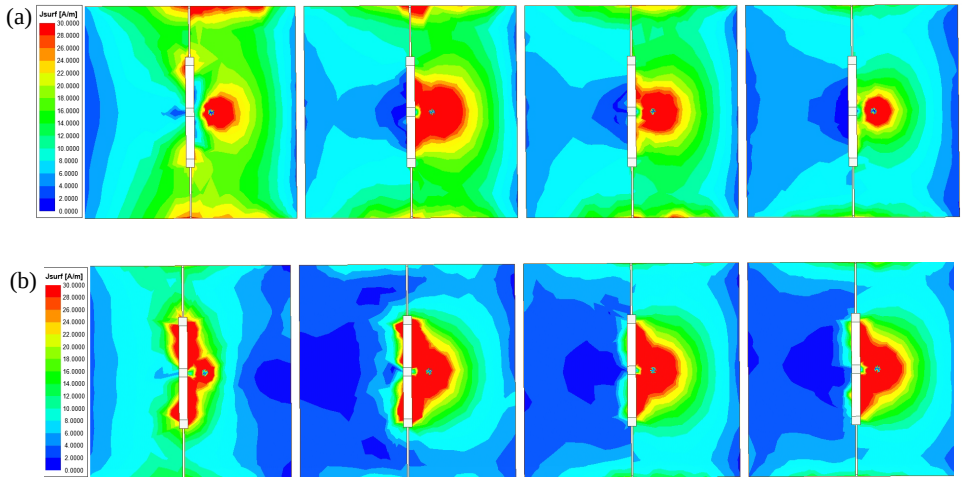

FIGURE 10. Simulated surface current distributions of the proposed array at 2.4 GHz. (a) Without an isolation slot. (b) With an isolation slot.

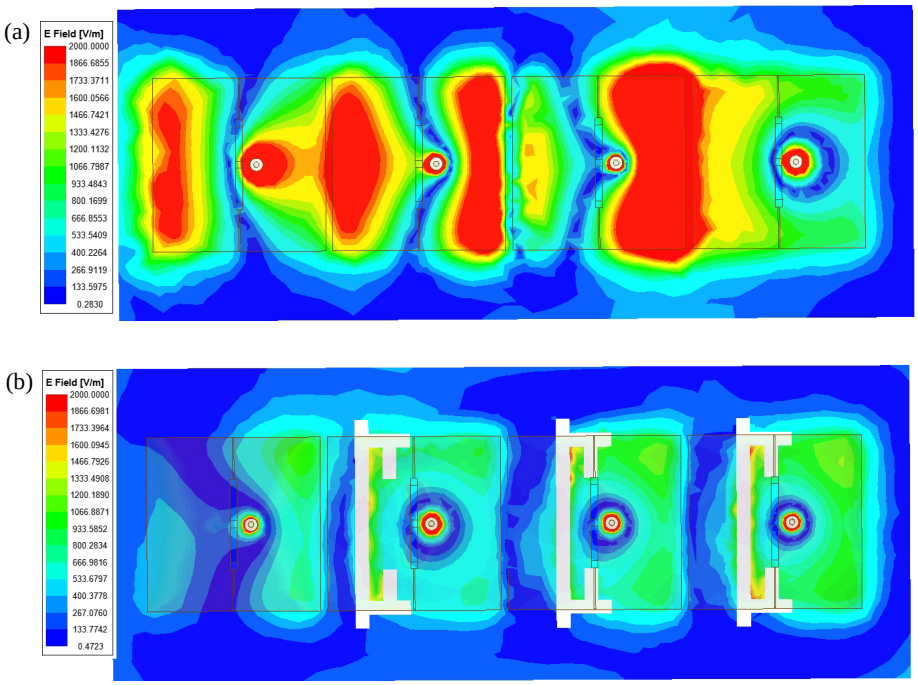

FIGURE 11. Simulated E-field distributions of the proposed array at 2.4 GHz. (a) Without an isolation slot. (b) With an isolation slot.

resonance mechanism. This separation of field-control regions, where the patch-top for reconfigurability and ground-plane is designed for isolation, allows the MIMO array to maintain continuous high-band tuning from 3.3 GHz to 4.6 GHz while ensuring strong suppression of inter-element coupling. This design provides a practical and scalable solution for multi-band tunable MIMO systems, where compactness and frequency agility must be achieved simultaneously.

4. MEASUREMENT OF THE MIMO ANTENNA DESIGN

To experimentally validate the performance of the proposed reconfigurable dual-band MIMO antenna array, a prototype was fabricated and measured. Photographs of the realized structure are shown in Fig. 13, illustrating both the top radiating surface and the etched ground plane with the Π-shaped isolation slots. Standard FR4 substrate and commercially available varactor diodes were used to ensure consistent manufacturing quality and to replicate realistic implementation conditions. SMA connectors were soldered onto each feed line with careful grounding to minimize parasitic effects introduced by the measurement setup.

The antenna was characterized using a vector network analyzer (VNA) for S-parameter measurements, and a fully anechoic chamber was employed for radiation pattern and gain evaluation, as shown in Fig. 14. Prior to testing, a full two-port calibration was performed to ensure accuracy across the operating bands. DC bias voltages were supplied through an

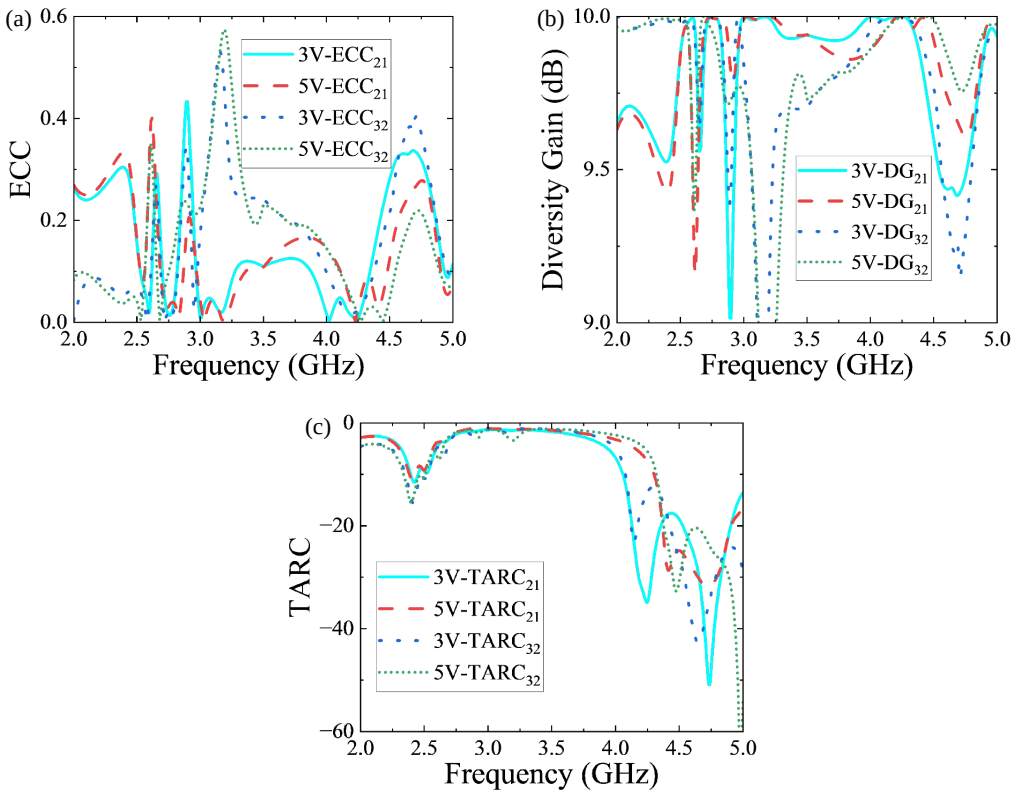

FIGURE 12. MIMO metrics of the antenna under different DC bias voltages. (a) Envelope correlation coefficient. (b) Diversity gain. (c) Total active reflection coefficient.

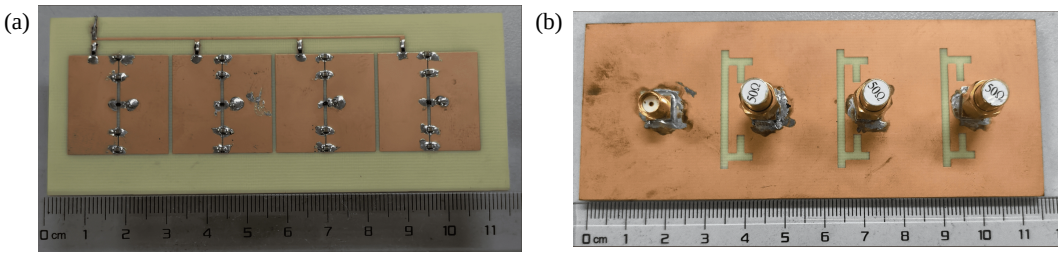

FIGURE 13. Photographs of the fabricated MIMO antenna array. (a) Top side. (b) Back view.

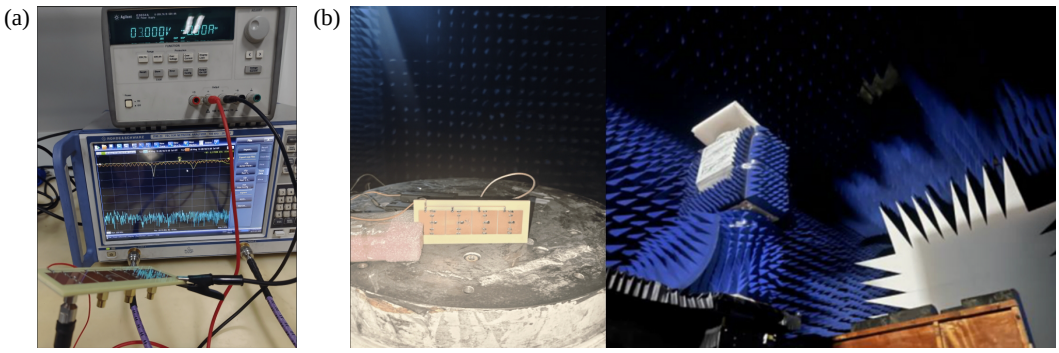

FIGURE 14. Measurement of the MIMO antenna array. (a) S-parameter measurement. (b) Radiation pattern measurement.

external bias network consisting of high-impedance RF chokes and bypass capacitors, guaranteeing minimal interference with the RF path during measurement.

Figure 15 presents the measured return losses of the MIMO antenna at different DC bias voltages. The results confirm that the low-frequency band remains centered near 2.3–2.4 GHz

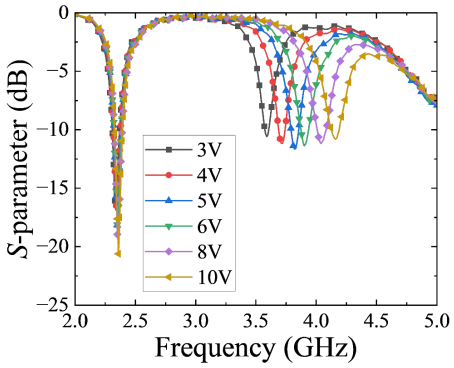

FIGURE 15. Measured S-parameters of the MIMO antenna at Port 1.

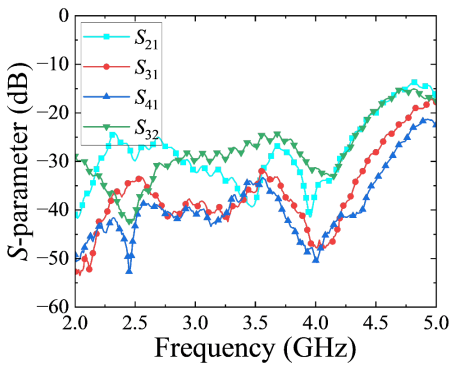

FIGURE 16. Measured S-parameters of the MIMO antenna under the bias voltage of 3 V.

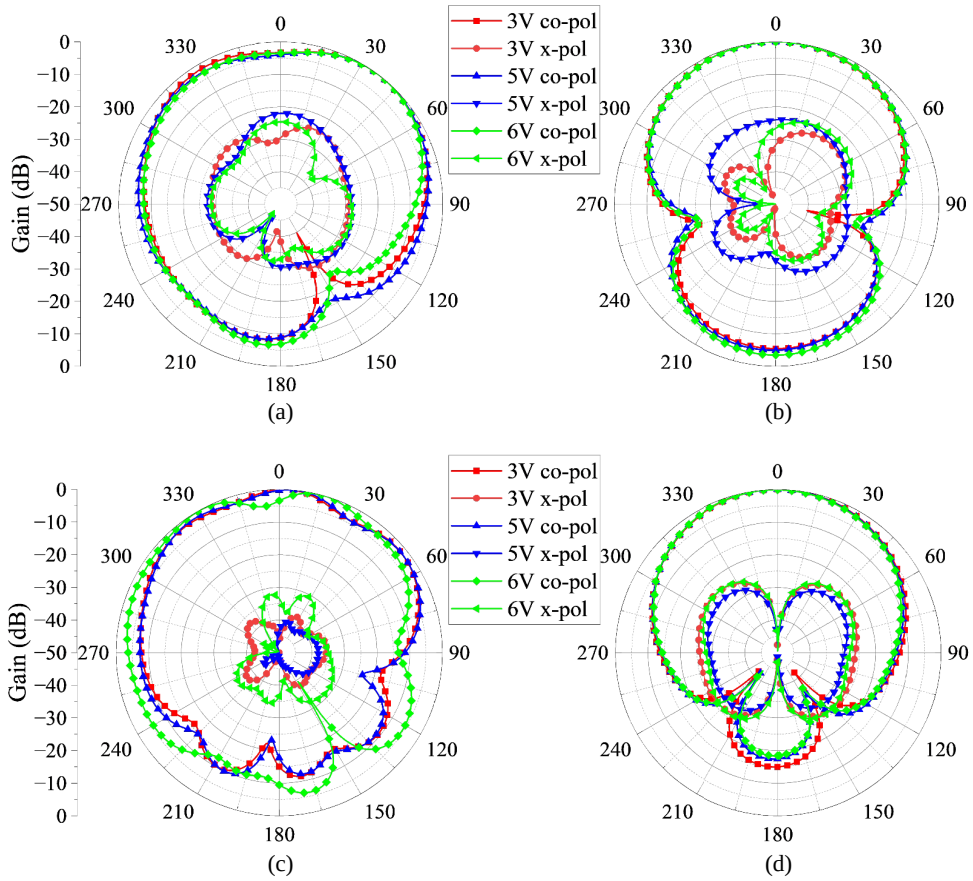

FIGURE 17. Measured normalized radiation patterns of the MIMO antenna at Port 1. (a) At 2.4 GHz in *xoz*-plane. (b) At 2.4 GHz in *yoz*-plane. (c) At 3.6 GHz (3 V), 3.8 GHz (5 V), 3.9 GHz (6 V) in *xoz*-plane. (d) At 3.6 GHz (3 V), 3.8 GHz (5 V), 3.9 GHz (6 V) in *yoz*-plane.

regardless of bias changes, demonstrating the stability of the lower resonance mode and validating the effectiveness of the capacitive bridging structure. Meanwhile, the high-frequency resonant mode shifts upward as the bias increases, corresponding to the decreasing capacitance of the varactor diodes. The measured tuning range of 3.6–4.2 GHz agrees well with simulation, confirming that the varactor-controlled reconfigurability is preserved in the fabricated prototype.

Isolation performance was also examined. Fig. 16 shows representative transmission coefficients (S_{21}, S_{31}, S_{41}) under a 3-V bias. The measured isolation exceeds 20 dB for both frequency bands, with minimum values of -24.1 dB at 2.33 GHz and -27.8 dB at 3.65 GHz. These results validate the effectiveness of the Π-slot isolation structure, which consistently suppresses surface-wave coupling even when the high-band resonance is tuned.

Radiation patterns measured at 2.4 GHz and at high-band resonances under different bias voltages are plotted in Fig. 17. Good agreement with simulated patterns is observed, confirming stable broadside radiation characteristics. At 2.4 GHz, the antenna exhibits symmetrical patterns with low cross-polarization levels in both principal planes. At high

TABLE 3. Comparison between the proposed antenna and existing research.

Ref.	Center Frequency (GHz)	Antenna Size ($\lambda_o \times \lambda_o$)	Decoupling Method	Reconfigurability	Isolation (dB)	Isolation Improvement (dB)	ECC
[18]	2.5	1.08×0.82	L-shaped stub & DGS	No	> 35	15	< 0.02
[26]	3.8	0.08×0.08	U-shaped DGS	No	> 14.5	4	< 0.02
[28]	3.4	0.51×0.51	DGS	No	> 15	6	< 0.01
[30]	5.9	1.46×1.46	Parasitic elements & DGS	No	> 33	12	< 0.001
This Work	2.4/3.3–4.6	0.30×0.30	Π-shaped DGS	Yes	> 24	15	< 0.02

frequencies, the main beam remains directed normal to the patch surface with only slight variations caused by tuning-induced impedance changes. The measured peak gains reach 3.2 dBi and 5.3 dBi at the low and high bands, respectively. Additionally, radiation efficiency improves with increasing bias voltage due to reduced varactor series resistance at higher reverse-bias levels.

In Table 3, this design is compared with existing related works in detail. The comparison results indicate that the proposed frequency-reconfigurable MIMO antenna array offers distinct advantages: Firstly, the frequency-reconfigurable feature enhances the practicality of the design, enabling it to operate efficiently in scenarios with varying frequency requirements. Secondly, the proposed structural decoupling solution ensures that the isolation performance of the antenna is significantly improved during the frequency tuning process.

5. CONCLUSION

This work has presented a compact dual-band reconfigurable MIMO antenna array that effectively addresses the conflicting requirements of frequency agility and inter-element isolation in space-constrained wireless platforms. By integrating a slit-loaded patch structure with varactor-based tuning, the antenna achieves stable low-band performance while enabling continuous high-band frequency reconfiguration. To overcome the strong coupling typically introduced by dense integration and tuning components, an innovatively engineered Π-shaped ground-plane slot structure was incorporated. The proposed isolation mechanism successfully suppresses dominant surface-wave coupling paths across all tuning states, ensuring high port-to-port isolation without compromising impedance matching or radiation characteristics. Extensive simulations and experimental measurements verified the effectiveness of the design. The fabricated prototype demonstrated a stable low-frequency resonance near 2.3–2.4 GHz, a wide high-band tuning range from 3.6 to 4.2 GHz, and isolation levels consistently exceeding 20 dB. Additionally, low ECC values and favorable gain performance confirm the array's suitability for high-capacity MIMO applications. Overall, the proposed architecture provides a practical and robust solution for adaptive wireless systems where compactness, spectral flexibility, and strong isolation are simultaneously required. Future work may explore using low-loss substrates, higher-Q tuning components, or metamaterial-inspired miniaturization techniques to further enhance efficiency and extend the reconfigurable bandwidth.

ACKNOWLEDGEMENT

This work was supported in part by the National Natural Science Foundation of China under Grant 62301267 and in part by the Natural Science Foundation of Jiangsu Province under Grant BK20230414.

REFERENCES

[1] Agiwal, M., A. Roy, and N. Saxena, "Next generation 5G wireless networks: A comprehensive survey," *IEEE Communications Surveys & Tutorials*, Vol. 18, No. 3, 1617–1655, 2016.

[2] Guo, J., C.-K. Wen, S. Jin, and G. Y. Li, "Overview of deep learning-based CSI feedback in massive MIMO systems," *IEEE Transactions on Communications*, Vol. 70, No. 12, 8017–8045, Dec. 2022.

[3] Nguyen, D. C., M. Ding, P. N. Pathirana, A. Seneviratne, J. Li, D. Niyato, O. Dobre, and H. V. Poor, "6G Internet of Things: A comprehensive survey," *IEEE Internet of Things Journal*, Vol. 9, No. 1, 359–383, Jan. 2022.

[4] Agnelli, F., G. Albasini, I. Bietti, A. Gnudi, A. Lacaita, D. Manstretta, R. Rovatti, E. Sacchi, P. Savazzi, F. Svelto, E. Temporiti, S. Vitali, and R. Castello, "Wireless multi-standard terminals: System analysis and design of a reconfigurable RF front-end," *IEEE Circuits and Systems Magazine*, Vol. 6, No. 1, 38–59, 2006.

[5] Sun, L., Y. Li, Z. Zhang, and H. Wang, "Self-decoupled MIMO antenna pair with shared radiator for 5G smartphones," *IEEE Transactions on Antennas and Propagation*, Vol. 68, No. 5, 3423–3432, May 2020.

[6] Serghiou, D., M. Khalily, V. Singh, A. Araghi, and R. Tafazolli, "Sub-6 GHz dual-band 8×8 MIMO antenna for 5G smartphones," *IEEE Antennas and Wireless Propagation Letters*, Vol. 19, No. 9, 1546–1550, Sep. 2020.

[7] Sahu, L. K., P. K. Gupta, S. Kharche, B. Mukherjee, and R. Tiger, "Design and analysis of four element MIMO antenna for broad-

band applications," *International Journal of Applied Electromagnetics and Mechanics*, Vol. 77, No. 4, 291–298, 2025.

[8] Yuan, X.-T., Z. Chen, T. Gu, and T. Yuan, "A wideband PIFA-pair-based MIMO antenna for 5G smartphones," *IEEE Antennas and Wireless Propagation Letters*, Vol. 20, No. 3, 371–375, Mar. 2021.

[9] Li, W., W. Lin, and G. Yang, "A compact MIMO antenna system design with low correlation from 1710 MHz to 2690 MHz," *Progress In Electromagnetics Research*, Vol. 144, 59–65, 2014.

[10] Ananta, R. A., M. A. Haque, G. Alyami, M. S. Ahammed, M. K. Ahmed, N. S. S. Singh, M. A. Rahman, H. Shaman, H. A. Abdallah, and A. A. Ateya, "Regression machine learning-based highly efficient dual band MIMO antenna design for mm-Wave 5G application and gain prediction," *Scientific Reports*, Vol. 15, No. 1, 28730, 2025.

[11] Khidre, A., F. Yang, and A. Z. Elsherbeni, "A patch antenna with a varactor-loaded slot for reconfigurable dual-band operation," *IEEE Transactions on Antennas and Propagation*, Vol. 63, No. 2, 755–760, Feb. 2015.

[12] Wu, Y. and H. Sun, "A low-profile wideband omnidirectional antenna with reconfigurable tri-polarization diversity," *AEU — International Journal of Electronics and Communications*, Vol. 176, 155149, 2024.

[13] Bonthu, M. K., A. K. Sharma, and N. Gupta, "An investigation of dual-band frequency tunable microstrip antenna for 5G and GPS applications," *International Journal of Applied Electromagnetics and Mechanics*, Vol. 79, No. 1, 38–47, 2025.

[14] Zhu, W., L. Wang, and Z. Yi, "Novel frequency-reconfigurable and self-decoupling technique for MIMO antenna systems leveraging flexible air cavities," *IEEE Antennas and Wireless Propagation Letters*, Vol. 24, No. 9, 3104–3108, 2025.

[15] Kulkarni, S. and A. Kunte, "Design of V-cut patch MIMO antenna for the 5.4 GHz band," *Wireless Personal Communications*, Vol. 121, No. 4, 3233–3242, 2021.

[16] Kim-Thi, P., T. N. Van, and T. B. Thanh, "A self-decoupling technique for isolation enhancement in closely-spaced MIMO patch antennas," *IEEE Antennas and Wireless Propagation Letters*, Vol. 23, No. 6, 1695–1699, Jun. 2024.

[17] Yang, Q., C. Zhang, Q. Cai, T. H. Loh, and G. Liu, "A MIMO antenna with high gain and enhanced isolation for WLAN applications," *Applied Sciences*, Vol. 12, No. 5, 2279, 2022.

[18] Li, Y., L.-A. Bian, K.-D. Xu, Y. Liu, Y. Wang, R. Chen, and S. Xie, "Mutual coupling reduction for monopole MIMO antenna using L-shaped stubs, defective ground and chip resistors," *AEU — International Journal of Electronics and Communications*, Vol. 160, 154524, Feb. 2023.

[19] Sui, J., C. Huang, J. Li, X. Zhu, and D. Li, "Wideband aperture-overlapped MIMO antennas naturally integrating mode orthogonal and parasitic decoupling schemes," *IEEE Antennas and Wireless Propagation Letters*, Vol. 23, No. 8, 2441–2445, 2024.

[20] Munusami, C. and R. Venkatesan, "A compact boat shaped dual-band MIMO antenna with enhanced isolation for 5G/WLAN application," *IEEE Access*, Vol. 12, 11 631–11 641, 2024.

[21] Güler, C. and S. E. B. Keskin, "A novel high isolation 4-port compact MIMO antenna with DGS for 5G applications," *Micromachines*, Vol. 14, No. 7, 1309, 2023.

[22] Abdullah, M., S. H. Kiani, N. Shoaib, T. Ali, H. Elmannai, A. D. Algarni, and U. F. Khattak, "An eight element wideband DGS MIMO antenna system for 5G handheld devices," *IEEE Access*, Vol. 12, 141 476–141 488, 2024.

[23] Kulkarni, N. P., N. B. Bahadure, P. D. Patil, and J. S. Kulkarni, "Flexible interconnected 4-port MIMO antenna for sub-6 GHz 5G and X band applications," *AEU — International Journal of Electronics and Communications*, Vol. 152, 154243, 2022.

[24] Tran-Huy, H., H. N. Tuan, N. Q. Dinh, D.-N. Tran-Viet, and H.-C. Park, "Multi-element self-decoupled MIMO patch antenna with flexible characteristics," *IEEE Access*, Vol. 12, 21 569–21 575, 2024.

[25] Wei, C. Y., H. C. Zhang, L. Xiao, and T. J. Cui, "Adaptive reduction of mutual coupling between compact frequency-reconfigurable antennas using tunable slow-wave structures," *IEEE Antennas and Wireless Propagation Letters*, Vol. 24, No. 7, 1699–1703, Jul. 2025.

[26] Abdullah, M., S. H. Kiani, N. Shoaib, T. Ali, H. Elmannai, A. D. Algarni, and U. F. Khattak, "An eight element wideband DGS MIMO antenna system for 5G handheld devices," *IEEE Access*, Vol. 12, 141 476–141 488, 2024.

[27] Nej, S., S. K. Bairappaka, D. B. D. S. R. Ram, S. Jana, and A. Ghosh, "Design of a high order dual band MIMO antenna with improved isolation and gain for wireless communications," *Arabian Journal for Science and Engineering*, Vol. 50, No. 8, 5727–5744, 2025.

[28] Jayaraman, G., I. Singh, and D. K. Choudhary, "Minimised four-port MIMO antenna for sub-6 GHz and satellite applications," *Defence Science Journal*, Vol. 75, No. 3, 318–324, 2025.

[29] Zhao, X. and S. Riaz, "A dual-band frequency reconfigurable MIMO patch-slot antenna based on reconfigurable microstrip feedline," *IEEE Access*, Vol. 6, 41 450–41 457, 2018.

[30] Sufian, M. A., N. Hussain, A. Abbas, J. Lee, S. G. Park, and N. Kim, "Mutual coupling reduction of a circularly polarized MIMO antenna using parasitic elements and DGS for V2X communications," *IEEE Access*, Vol. 10, 56 388–56 400, 2022.

[31] Mshwat, W. F. A., J. S. Kosha, A. Salisu, A. Ullah, N. T. Ali, I. Elfergani, C. H. See, C. Zebiri, J. Rodriguez, and R. Abd-Alhameed, "Compact reconfigurable MIMO antenna for 5G and Wi-Fi applications," *IEEE Access*, Vol. 12, 110 283–110 298, 2024.